

Optimal recovery manoeuvres of racing motorcycles

E. Marconi · M. Massaro

Received: date / Accepted: date

Abstract The focus of this work is on the optimal recovery manoeuvres of racing vehicles, which are here defined as the manoeuvres that need be performed in order to complete the lap in the minimum time, after a driving error occurs. The driving errors considered are speed excess and trajectory deviations, with respect to the baseline conditions. The baseline conditions are those giving the minimum lap time, and are vehicle and track dependent. The practical applications of the methodology proposed include the estimation of the driving errors that can be recovered while remaining within the racetrack borders, and the estimation of the minimum asphalted run-off area that need be provided to recover from driving errors of given magnitude. An example of application is given for a racing motorcycle on the Mugello circuit.

Keywords motorcycle · recovery · three-dimensional road · lap time · minimum time · optimal control · vehicle dynamics

1 Introduction

Optimal control techniques have been used extensively in the literature to predict the minimum-time manoeuvring of road vehicles, both in the case of cars and motorcycles [1–18]. The typical set-up includes the definition of the circuit geometry (curvatures, width, etc.) and the vehicle characteristics (mass, tyres, engine, etc.). The simulation aims at the computation of the minimum lap time, together with the associate states (speed, trajectory, etc.) and controls

E. Marconi
Department of Industrial Engineering, University of Padova, Via Venezia 1, 35131 Padova

M. Massaro
Department of Industrial Engineering, University of Padova, Via Venezia 1, 35131 Padova
Tel.: +39-049-827-6792
E-mail: matteo.massaro@unipd.it

(steering, throttle, etc.). The literature have shown that the minimum-time simulations are generally in good agreement with the manoeuvres actually performed by race drivers.

Much less explored is the application of optimal control techniques to the computation of recovery manoeuvres, which are the manoeuvres performed after a driving error, in order to ‘recover’ the vehicle and rejoin the ideal driving path. In passenger cars, driving errors often lead to the so-called ‘terminal understeer’ condition, where the driver cannot follow the desired path with the available tyre-road friction. As a consequence, a recovery manoeuvre is necessary. Different recovery manoeuvres can be considered, depending on the objective that the driver is pursuing. In the context of racing scenarios, it is reasonable to assume that the drivers will attempt to recover in order to complete the lap in the minimum time, hence the idea of employing minimum-time techniques to simulate such recovery manoeuvres.

We thus define the ‘optimal recovery manoeuvre’ as the manoeuvre that need be performed in order to complete the lap in the minimum time, after a driving error has occurred. The resulting recovery trajectory may be far different from the ideal (baseline) trajectory – the trajectory obtained while traversing the circuit in the minimum time without errors – although in general the recovery manoeuvre becomes coincident with the baseline manoeuvre after a certain distance has been travelled. Such distance depends on the circuit, vehicle and driving error.

The best performance of the vehicle is basically obtained following the optimal trajectory with the optimal speed profile. Therefore, variations with respect to such references can be considered errors, since race riders always aim at the best performance. A speed excess may occur e.g. at turn entry, when the rider misses the braking point (i.e. starts braking too late), e.g. because of a lack of concentration or in an attempt to defend from or complete an overtake. Similarly, following a path different from the ideal racing line is a possible strategy to gain an advantage in ‘wheel-to-wheel’ fights. In this work, the considered driving errors consist in a speed excess while on the baseline trajectory and trajectory deviations while travelling at the baseline speed, along with the combination of the two.

The potential application of the method is the assessment of the driving errors that can be recovered while remaining within the racetrack borders (or run-off areas), and the determination of the minimum asphalted area surrounding a racetrack that need be provided to recover driving errors of a given magnitude.

The focus of the investigation is on motorcycles, which are especially challenging from the dynamic point of view [5, 19, 20]. However, the same approach is applicable to cars as well. An example of application of the method is given on the Mugello circuit, whose three-dimensional geometry is available from the literature [21, 22]. The characteristics of the motorcycle are also taken from the literature [21, 22], and are representative of a 1000cc racing bike. The dynamic vehicle model is an extension of the advanced model employed in [22], the main difference being the modelling of the tyre structural compliance, which

is now divided into radial and lateral, instead of a single stiffness normal to the road – indeed the effective tyre stiffness normal to the road changes with camber, which may reach 60 deg in racing applications.

A notable application of optimal control to the recovery from driving errors is given in [23–25], where the mitigation of terminal understeer via integrated brake control is discussed. Terminal understeer is the situation in which the available lateral acceleration is not sufficient for the vehicle to follow a desired path. This occurs when the speed at turn entry is too high with respect to the required path curvature, given the prevailing tyre-road friction. The recovery from terminal understeer is formulated as a free-final-time optimal control problem, in which the objective is to minimize the maximum off-tracking (i.e. the deviation) from the reference path. The optimal control problem related to a circular reference path is solved for both a friction-limited point-mass vehicle model and a two-track vehicle model with a non-linear combined-slip tyre model and load transfer effects. The trajectories and speed profiles found in the two cases are quite close, and correspond exactly to a parabola in the point-mass case. The optimal control solution is used to develop a closed-loop controller for understeer mitigation through braking control, taking into account the driver's steering input. An automated emergency cornering system, aimed at avoiding lateral deviation leading to lane or road departure, is introduced in [26]. Motion planning is performed by an upper-level controller that employs a non-linear friction-limited particle model. Previous results [23, 25] – obtained for a circular reference path – are extended to a more general road geometry using a geometric analysis. A lower-level controller governs the available actuators according to the planned motion, using a planar two-track seven-degree-of-freedom vehicle model with simplified Magic Formula tyres. The track model used in the controller comprises a horizontal, flat road surface model. The controller requires a digital map with road geometry and friction information.

It is worth noting that the recovery strategy in [23–26] aims to minimize the maximum off-tracking deviation, while in this work the recovery strategy aims to minimize the manoeuvre time. In addition, in this work the recovery manoeuvres are triggered by speed errors and trajectory deviations, which are not necessarily generated by a terminal understeer condition.

The work is organised as follows. In Sec. 2 the vehicle, tyre and road models are described. In Sec. 3 the optimal control problem is formulated. The baseline lap simulation is discussed in Sec. 4, while the set-up of the recovery simulations is described in Sec. 5. The application of the methodology to the Mugello circuit is presented in Sec. 6, where the analysis of the existing paved run-off areas is also addressed.

2 Mathematical model

The numerical model employed for all the simulations in this work consists of the combination of a dynamic vehicle model, a tyre model and a three-

dimensional road model. The key features are illustrated in the following sections.

2.1 Vehicle model

The vehicle model employed in this work is derived from the motorcycle model used by the authors in [8, 22]. It consists of four rigid bodies (the main chassis with a rigidly attached rider, the front assembly, the front and the rear wheels), and has nine degrees of freedom (DOFs): the chassis position and orientation (6 DOFs), the steering angle (1 DOF) and the suspension travels (2 DOFs).

The vehicle model is described by 20 first-order implicit ordinary differential equations of the form:

$$\mathbf{f}(\mathbf{x}, \dot{\mathbf{x}}, \mathbf{u}) = \mathbf{0}, \quad (1)$$

where \mathbf{x} is the vector of state variables and \mathbf{u} is the vector of controls. The state variables are:

$$\mathbf{x} = [s, n, \xi, V_x, V_y, \dot{\psi}, \varphi, \dot{\varphi}, \sigma, \dot{\sigma}, z, \dot{z}, \delta, \dot{\delta}, z_f, \dot{z}_f, z_r, \dot{z}_r, \varepsilon_{L,f}, \varepsilon_{L,r}]^T, \quad (2)$$

where s is the travelled distance along the track centreline, n is the lateral deviation with respect to the centreline, ξ is the relative orientation with respect to the tangent to the centreline, V_x and V_y are the longitudinal and lateral velocities of the centre of mass, $\dot{\psi}$ is the vehicle yaw rate, φ is the vehicle camber angle, σ is the vehicle pitch angle, z is the vertical displacement of the centre of mass, δ is the steering angle, z_f and z_r are the front and rear suspension travels, and $\varepsilon_{L,f}$ and $\varepsilon_{L,r}$ are the lateral deflections of the front and rear tyres. The controls are:

$$\mathbf{u} = [\tau_h, F_{x,f}, F_{x,r}]^T, \quad (3)$$

where τ_h is the steering torque, and $F_{x,f}$ and $F_{x,r}$ are the front and rear tyre longitudinal forces.

The stiffness and damping of suspensions are modelled with polynomial functions of the suspension travels and rates. The model accounts for the effects of the chain final transmission. For simplicity, the upper chain run is assumed in tension when accelerating while the chain is assumed slack when braking (i.e. there is no engine braking).

2.2 Tyre model

The tyre model takes into account the shape of the crown radius, which is assumed toroidal. The steady-state lateral tyre forces F_y^0 depend linearly on the lateral slip α and camber γ angles:

$$\begin{aligned} F_{y,f}^0 &= (k_{\alpha,f}\alpha_f + k_{\gamma,f}\gamma_f) N_f, \\ F_{y,r}^0 &= (k_{\alpha,r}\alpha_r + k_{\gamma,r}\gamma_r) N_r, \end{aligned} \quad (4)$$

where the subscripts f and r indicate the front and rear tyre, k_α and k_γ are the lateral slip and camber tyre stiffness (per unit normal load) respectively, and N is the tyre vertical load. The structural compliance of the tyres is represented by two flexibilities: a radial stiffness k_R and a lateral stiffness k_L .

Tyre relaxation (i.e. the well-known lag in the generation of tyre lateral forces) is modelled through a balance between the component in the road plane of the elastic force due to the deformation of the two tyre springs and the tyre lateral force generated by sideslip and camber [5, 27–29]:

$$\begin{aligned} F_{y,f} &= +k_{L,f}\varepsilon_{L,f} \cos \gamma_f - k_{R,f}\varepsilon_{R,f} \sin \gamma_f, \\ F_{y,r} &= +k_{L,r}\varepsilon_{L,r} \cos \gamma_r - k_{R,r}\varepsilon_{R,r} \sin \gamma_r, \end{aligned} \quad (5)$$

where ε_L and ε_R are the deformations of the tyre lateral and radial springs respectively. The left-hand side of equation (5) represents the instantaneous or relaxed lateral tyre force, which is calculated using (4) with the instantaneous lateral slip α_i . This is the slip computed while accounting for the deflections of the carcass ε_L and ε_R [5, 27–29]:

$$\tan \alpha_i = \frac{V_{C,y} + \dot{\varepsilon}_L \cos(\gamma) - \dot{\varepsilon}_R \sin(\gamma) - \dot{\gamma} [(z_0(\gamma) + \varepsilon_R) \cos(\gamma) + (y_0(\gamma) + \varepsilon_L) \sin(\gamma)]}{V_{C,x} + \dot{\varpi} [(z_0(\gamma) + \varepsilon_R) \sin(\gamma) - (y_0(\gamma) + \varepsilon_L) \cos(\gamma)]}, \quad (6)$$

where $V_{C,x}$ and $V_{C,y}$ are the longitudinal and lateral components of the velocity of the wheel centre, ϖ and γ are the wheel yaw and camber angle respectively ($\varpi = \psi$ and $\gamma = \varphi$ for the rear wheel, while additional terms related to the steering angle are needed for the front wheel). The functions $z_0(\gamma)$ and $y_0(\gamma)$ express the shape of the tyre cross section; for the toroidal shape here considered:

$$z_0(\gamma) = R + \rho (\cos \gamma - 1), \quad (7a)$$

$$y_0(\gamma) = \rho \sin \gamma. \quad (7b)$$

where R is the (unloaded) tyre radius and ρ is the radius of the tyre cross section.

The tyre vertical load is also expressed as a function of tyre deformations:

$$\begin{aligned} N_f &= -k_{L,f}\varepsilon_{L,f} \sin \gamma_f - k_{R,f}\varepsilon_{R,f} \cos \gamma_f, \\ N_r &= -k_{L,r}\varepsilon_{L,r} \sin \gamma_r - k_{R,r}\varepsilon_{R,r} \cos \gamma_r. \end{aligned} \quad (8)$$

The radial tyre deformations are computed by requiring the tyre contact points to lie on the road surface:

$$z_{CP,f}(\mathbf{x}, \varepsilon_{R,f}) = 0, \quad z_{CP,r}(\mathbf{x}, \varepsilon_{R,r}) = 0, \quad (9)$$

where $z_{CP,f}$ and $z_{CP,r}$ are the coordinates of the front and rear contact points normal to the road plane. Pure rolling is assumed in the longitudinal direction.

The coupling between lateral and longitudinal tyre forces is accounted for using friction ellipses, which saturate tyre forces:

$$\frac{\left(\frac{F_{x,f}}{\mu_{x,f}}\right)^2 + \left(\frac{F_{y,f}}{\mu_{y,f}}\right)^2}{N_f^2} \leq 1, \quad \frac{\left(\frac{F_{x,r}}{\mu_{x,r}}\right)^2 + \left(\frac{F_{y,r}}{\mu_{y,r}}\right)^2}{N_r^2} \leq 1, \quad (10)$$

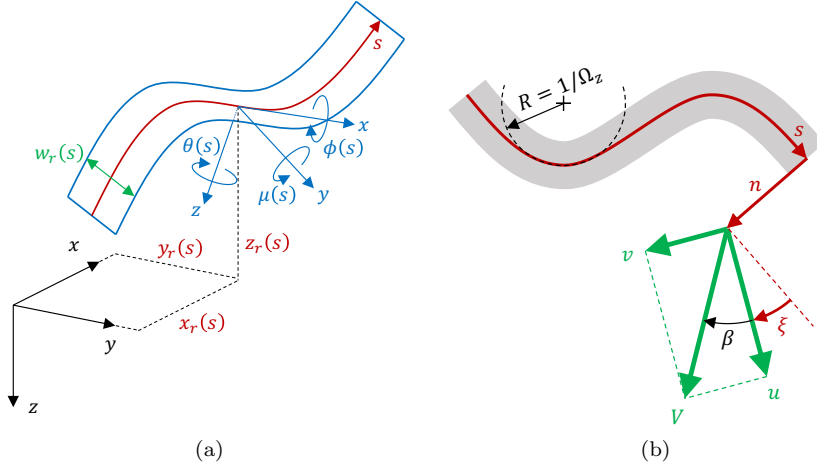


Fig. 1: Road representation. (a) Definition of the three-dimensional road model. (b) Vehicle position on the track based on curvilinear coordinates.

where F_x is the tyre longitudinal force, and μ_x and μ_y are the longitudinal and lateral friction coefficients.

2.3 Road model

The three-dimensional road is modelled following the approach presented in [5, 1]. The road is represented as a ribbon, with orientation and width that vary along its length. Each transverse section of the road is considered a straight line, i.e. the banking does not vary while moving laterally along each strip.

As shown in Fig. 1a, the road ribbon is characterised by the coordinates of its centreline (x_r , y_r , z_r), its orientation (heading, slope and banking), and its width (w_r), which are given functions of the curvilinear abscissa s , i.e. the distance travelled from the start/finish line along the road centreline. The road orientation is obtained from a fixed ‘ground frame’ through three consecutive rotations that represent the road heading (rotation about the z axis of angle θ), the road longitudinal slope (rotation about the y axis of angle μ), and the road banking (rotation about the x axis of angle ϕ). The centreline coordinates and road angles define the origin and orientation of the road reference frame, known as *Darboux frame*. This trihedron moves along the road centreline with the vehicle, and its x - y plane represents the road tangent plane. The road geometry can be effectively described through the definition of three curvatures: the geodesic curvature Ω_z (i.e. the curvature in the road tangent plane x - y), the normal curvature Ω_y (i.e. the curvature in the road sagittal plane x - z), and the relative torsion Ω_x . These quantities correspond to the components of the angular rate – angle per unit length – of the road reference frame, expressed in the road frame itself.

The position of the vehicle on the road is obtained by using the curvilinear coordinates depicted in Fig. 1b, i.e. the curvilinear abscissa s (travelled distance), the lateral displacement relative to the road centreline n , and the relative heading ξ with respect to the tangent to the road centreline. The reference point of the vehicle is the projection of the centre of mass on the road along the symmetry plane.

3 Optimal control problem

The non-linear optimal control problem (OCP) aimed at the computation of the minimum-time manoeuvre is solved using the indirect collocation algorithm PINS described in [14]. However, the formulation presented is suitable for solution with direct collocation methods as well [7].

The problem is defined in the space domain instead of the time domain. This results in a fixed integration domain – equal to the length of the considered track section – and is beneficial for numerical convergence [1]. The cost function of the OCP is the manoeuvre time, which can be written as

$$J = \int_{s_0}^{s_e} \frac{1}{\dot{s}} ds, \quad (11)$$

where $L = s_e - s_0$ is the length of the section of the track being considered and $\dot{s} = ds/dt$.

Inequality constraints are added to the optimal-control formulation to account for the physical limitations of the system, e.g. the technical limits of the vehicle and the limitations in rider inputs. In particular, these constraints include the maximum engine power

$$P \leq P_{\max}, \quad (12)$$

the maximum steering angle

$$|\delta| \leq \delta_{\max}, \quad (13)$$

the maximum steering torque

$$|\tau_h| \leq \tau_{h,\max}, \quad (14)$$

the minimum tyre vertical loads (to avoid the ‘wheelie’ and ‘stoppie’ conditions, in which the front and rear tyre respectively loses contact with the road)

$$N_f \geq 0, \quad N_r \geq 0, \quad (15)$$

the maximum tyre friction (represented by the friction ellipses in (10)), and road borders (i.e. the maximum lateral position on the track n , see Fig. 1b)

$$|n| \leq n_{\max}(s). \quad (16)$$

The maximum values employed in constraints (12)-(14) are reported in Table 1 in the appendix, while $n_{\max}(s)$ in (16) is given by the track geometry. The values are in line with those employed in [8, 21, 22].

Initial and final BCs are enforced through the following term which is added to the cost function in (11):

$$m(\mathbf{x}) = w_i \sum_{j=1}^{n_{\mathbf{x}}} k_{j,i} (x_j(s_i) - x_{j,i})^2 + w_f \sum_{j=1}^{n_{\mathbf{x}}} k_{j,f} (x_j(s_f) - x_{j,f})^2, \quad (17)$$

where w_i and w_f are weights (the higher their value, the more strictly the condition on initial/final states has to be satisfied), $n_{\mathbf{x}}$ is the number of state variables, x_j are the components of the vector of state variables \mathbf{x} , while $x_{j,i}$ and $x_{j,f}$ are the initial and final values required for the j -th state variable, and the coefficients $k_{j,i}$ and $k_{j,f}$ can be either 1 (BC enforced on the j -th state variable) or 0 (BC not enforced on the j -th state variable).

4 Baseline manoeuvre

A full-lap minimum-time simulation provides the baseline manoeuvre – the ‘clean lap’ – which is the reference on top of which the driving errors are added. This simulation is performed using cyclic boundary conditions, which means that the state variables at the beginning and at the end of the simulation (i.e. on the start/finish line) need be the same, the actual value being found by the solver in order to minimize the cost function (11). No BCs of the type in (17) are employed in this case, i.e. $w_i = w_f = 0$.

The results, presented in Fig. 2, are consistent with those reported in the literature [21, 22, 6]. The lap time is 104.457 s. The top speed – reached on the main straight – is 351.4 km/h, the maximum camber angle is 60.2 deg. The dataset is reported in the appendix. The numerical simulations are performed with a fixed mesh size of 0.7 m. The number of equations solved simultaneously for the full lap is approximatively 365,000.

5 Recovery manoeuvre simulations

The optimal recovery manoeuvres are here defined as the manoeuvres that need be performed in order to complete the lap in the minimum time, after a driving error occurs. Therefore, one needs to define (i) the locations where the driving errors are assumed to occur and (ii) the type of driving errors considered. These topics are discussed in the following two sections.

5.1 Track sections for recovery

The recovery manoeuvres originating from driving errors at turn entry are considered, since it is assumed that this is the phase where errors are most likely to occur and more challenging to recover.

For each turn, the following procedure is followed in order to identify the section where the recovery manoeuvres need be computed. The curvilinear

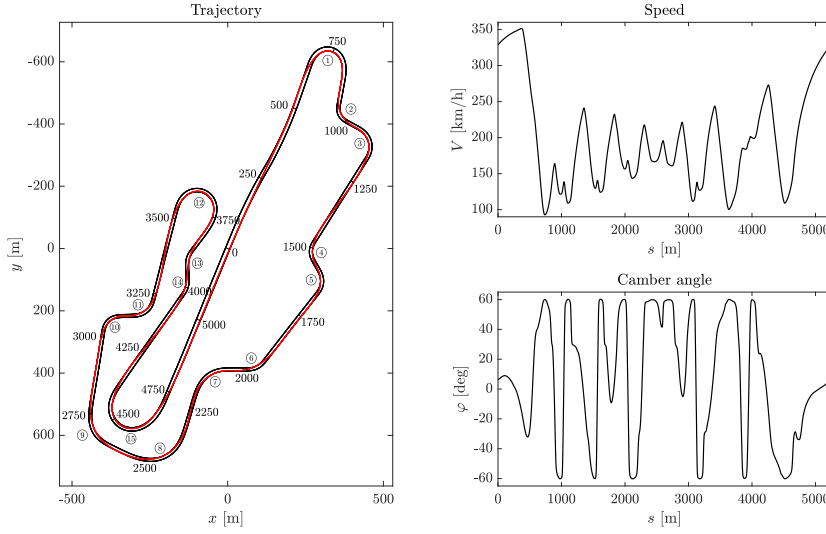


Fig. 2: Baseline full-lap simulation. The circuit map additionally shows the turn numbers (circled) and the distance travelled from the start/finish line.

abscissa where the recovery starts (s_i) is chosen within the interval $[s_1, s_2]$, where s_1 is the curvilinear abscissa where the vehicle starts turning in (which is here defined as the point where the lateral acceleration $a_y = V(\psi + \dot{\beta})$ exceeds $0.1g$), and s_2 is the curvilinear abscissa corresponding to the turn apex (which is here defined as the point where the longitudinal acceleration $a_x = \dot{V}$ is zero); $V = \sqrt{u^2 + v^2}$ (represented in Fig. 1b) is the velocity of the vehicle's reference point (which is the projection of the centre of mass of the vehicle on the road along the vehicle's symmetry plane), u and v being its components parallel and perpendicular to the intersection of the vehicle plane of symmetry with the ground, respectively.

The curvilinear abscissa where the recovery simulation ends (s_f) is determined so that the length of the recovery simulation is sufficient to complete the recovery manoeuvre, i.e. a set of variables of the recovery simulation match those of the baseline simulation. The selected variables are $\mathbf{x}^* = [n, \alpha, V, \varphi]^T$, which define the 'gross motion' of the vehicle (lateral position and relative orientation, speed and roll). The error E between the two simulations is evaluated by computing the 2-norm difference between the variables of the recovery simulation \mathbf{x}^* and the variables of the baseline simulation $\hat{\mathbf{x}}^*$ evaluated in corresponding locations along the track:

$$E(s) = \|\mathbf{x}^*(s) - \hat{\mathbf{x}}^*(s)\|_2. \quad (18)$$

The recovery manoeuvre is considered to have rejoined the baseline manoeuvre if there exists a track section of length l_0 in which the error is consistently lower

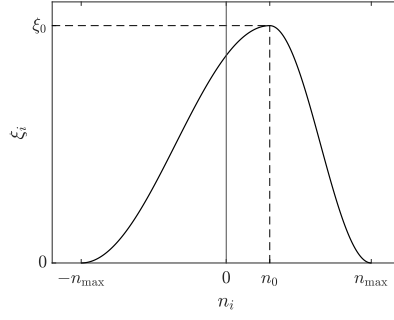


Fig. 3: Initial heading ξ_i as a function of the initial lateral position n_i .

than a fixed limit E_{\max} :

$$\exists \tilde{s} \quad : \quad E(s) \leq E_{\max} \quad \forall s \in [\tilde{s}, \tilde{s} + l_0]. \quad (19)$$

The procedure to determine s_f is repeated on each turn. As a rule of thumb, the recovery simulation must include at least the turn following the one where the driving error occurs.

5.2 Driving errors

Two types of driving errors are considered in this work. The first is a speed excess (with respect to the baseline manoeuvre), modelled by modifying the initial BC (17) related to the vehicle longitudinal speed V_x , while keeping all other initial BCs equal to their baseline value. The second driving error considered is a trajectory deviation (with respect to the baseline manoeuvre). In this case, the initial BC (17) related to the lateral position n is modified. When the modified initial lateral position n_i brings the trajectory close to the track borders, the trajectory need be parallel to the road, i.e. $\xi_i = 0$, assuming road width does not vary significantly. Therefore, it is chosen to change the initial relative vehicle heading ξ_i as a function of the initial lateral deviation n_i . The selected function is required to satisfy the following conditions:

$$\begin{cases} \xi_i(n_{\max}) = 0, \\ \xi_i(-n_{\max}) = 0, \\ \xi_i(n_0) = \xi_0, \end{cases} \quad (20)$$

where n_{\max} is the maximum lateral position on the track (equal to half of the road width), and ξ_0 and n_0 are the values of heading and lateral position in the baseline simulation at $s = s_i$. In other words, the initial relative vehicle heading ξ_i has to be zero on the track borders and equal to the one given by the baseline if no modification in the initial lateral position is enforced. Two

half-cosine curves are employed to build such function:

$$\xi_i(n_i) = \begin{cases} \frac{1}{2}\xi_0 \left(1 - \cos \frac{\pi(n_i + n_{\max})}{n_0 + n_{\max}} \right), & \text{if } -n_{\max} \leq n_i < n_0 \\ \frac{1}{2}\xi_0 \left(1 - \cos \frac{\pi(n_i - n_{\max})}{n_0 - n_{\max}} \right), & \text{if } n_0 \leq n_i \leq n_{\max}. \end{cases} \quad (21)$$

The resulting function, shown in Fig. 3, satisfies (20) and is continuous with continuous first derivative. Again, all other initial BCs are kept equal to their baseline value. The final states are left free, i.e. $w_f = 0$ in Eq. (17).

6 Example of application

The recovery manoeuvres arising from excessive speed and trajectory deviation at turn entry are now considered on the Mugello circuit – clearly the procedure can be applied to other circuits as well. The driving errors are computed with respect to the baseline manoeuvre in Sec. 4, according to the criteria defined in Sec. 5.

The two errors are initially considered separately, then their combined effect is discussed. The results are illustrated for Turn 1 (*San Donato*) – similar results are obtained for all the other turns of the circuit. The initial location s_i of the recovery simulations on Turn 1 ranges between $s = 550$ m and $s = 725$ m. The simulations were performed for s_i steps equal to 25 m: for the sake of conciseness, results are depicted for s_i steps of 50 m. During the recovery manoeuvres the vehicle is allowed to exceed the track borders, i.e. n_{\max} in (16) is made ‘large enough’ not to constrain the recovery trajectory. In addition, the tyre-road friction is kept constant when exceeding the track borders. In other words, it is assumed that there is a paved run-off area surrounding the track. Finally, kerbs are not considered.

6.1 Recovery from speed excess

The simulations consider a speed excess ΔV_i of up to 20 km/h (with 5 km/h steps) relative to the vehicle speed provided by the baseline full-lap simulation at $s = s_i$. Fig. 4 depicts the recovery trajectories on a plan view of the circuit. Magenta dots indicate the reference location (i.e. the point of the baseline trajectory) for each value of s_i . The higher the speed excess, the wider the recovery trajectory, as intuition suggests. The maximum lateral displacement of the recovery trajectories from the baseline occurs at roughly $s = 760$ m, i.e. about 30 m after the apex. Recovery trajectories starting from $s_i \geq 650$ m are completed within the track borders for all the values ΔV_i considered. On the other hand, for $s_i < 650$ m the recovery trajectories with $\Delta V_i = 20$ km/h wander out of the track, and hence require a paved run-off area to be completed. Thereby, for a given absolute speed error the recoveries with

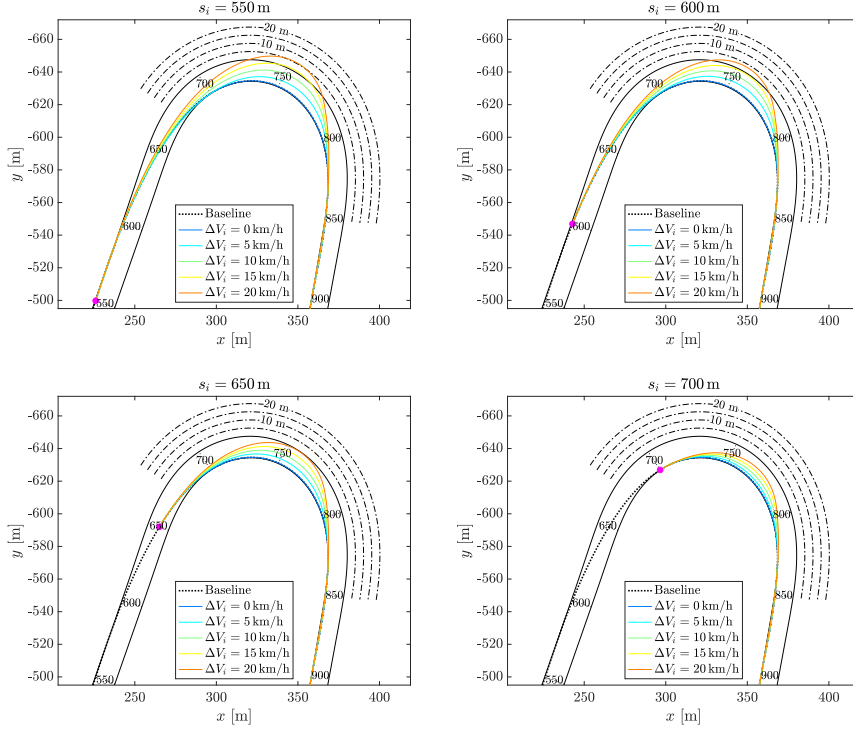


Fig. 4: Recovery trajectories from speed errors on the entry of Turn 1.

the rearmost starting locations are the most critical for the design of run-off areas, despite the relative initial speed excess being lower.

In order to gain a deeper insight into the dynamics of the recovery manoeuvres, Fig. 5 reports the speed and camber angle of the manoeuvres starting at $s_i = 650$ m. The recovery manoeuvres from higher speed errors result in ‘less round’ trajectories, characterised by lower minimum speeds mid corner and higher speeds at turn exit. In particular, the reduction of the rear tyre lateral force associated with the reduction of the camber angle around $s = 810$ m allows for a higher acceleration out of the turn, as the acceleration is friction-limited in that point. For the two highest speed errors considered ($\Delta V_i = 15, 20$ km/h) the tyre friction limit and the wheelie limit are reached simultaneously (while the camber angle is kept roughly constant, $\varphi = 30$ deg), and this condition actually corresponds to the maximum acceleration attainable when engine power is not the limiting factor. The maximum camber angle (60.1 deg) does not vary significantly between the recovery manoeuvres, but is reached later for higher ΔV_i values. As can be expected, the baseline manoeuvre ($\Delta V_i = 0$ km/h) corresponds to the minimum manoeuvre time, and the manoeuvre time increases with the speed excess. .

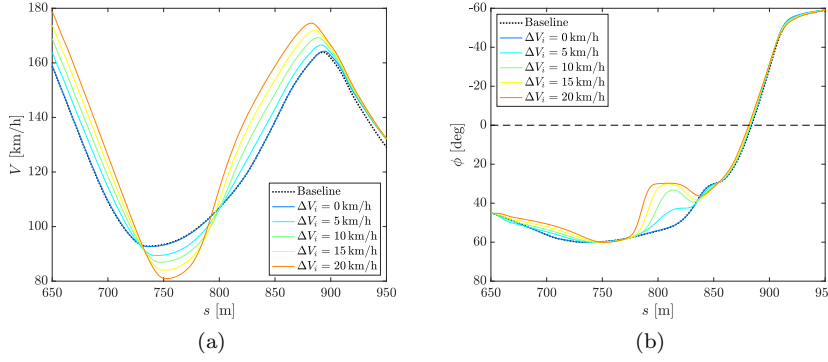


Fig. 5: Recovery dynamics from speed errors on the entry of Turn 1, $s_i = 650$ m. (a) Speed. (b) Camber angle.

6.2 Recovery from trajectory deviation

The simulations consider a trajectory lateral displacement Δn_i of up to 3 m (with 1 m steps) in either direction, relative to the vehicle position on the track provided by the baseline full-lap simulation at $s = s_i$. Clearly, trajectory displacements that bring the initial point outside of the track borders are discarded. Fig. 6 depicts the recovery trajectories on a plan view of the circuit. Magenta dots indicate the reference location (i.e. the point of the baseline trajectory) for each value of s_i . With both positive and negative values of Δn_i , the recovery trajectory is wider than the optimal reference mid corner. For a given $|n_i|$, the starting locations closer to the outer track border determine wider trajectories in the middle of the turn, see for instance the recovery trajectories for $s_i = 650$ m. As can be expected, the baseline manoeuvre ($\Delta n_i = 0$ m) corresponds to the minimum manoeuvre time, and manoeuvre time increases with the magnitude of the trajectory displacement $|n_i|$. Negative displacements (i.e. initial positions closer to the outer track borders) result in slightly higher manoeuvre times compared to the positive displacements of the same magnitude. With the focus on the design of run-off areas, the practical result is that none of the recovery trajectories arising from a perturbation in the trajectory requires a paved run-off area to be completed.

6.3 Combined effect of driving errors

In order to properly estimate the necessary paved run-off areas, combined speed and trajectory driving errors are analysed in this section. Fig. 7 considers trajectory displacements $\Delta n_i = 0, \pm 3$ m combined with speed excess values $\Delta V_i = 0, 10, 20$ km/h.

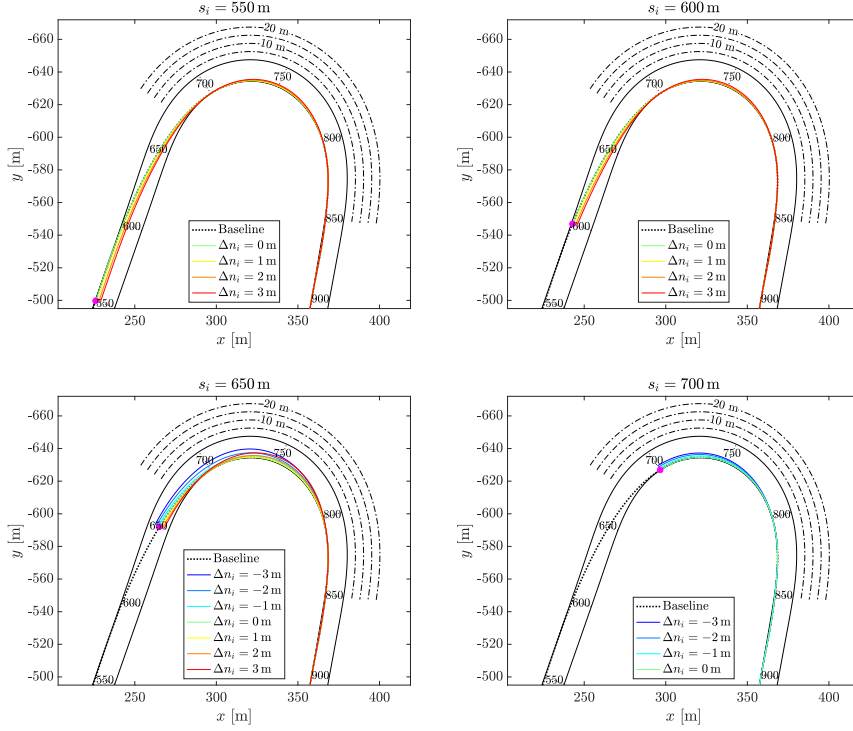


Fig. 6: Recovery trajectories from lateral position errors on the entry of Turn 1.

Fig. 7a shows the recovery trajectories starting from the rearmost location ($s_i = 550$ m), with a positive trajectory displacement (i.e. towards the inner track border). With the exception of the case $\Delta V_i = 0$ km/h, when a speed error is combined with a tighter position at turn entry, the trajectory in the middle of the corner results tighter compared to the recovery from the same speed excess and zero initial lateral displacement. Specifically, considering the case in which the recovery trajectory wanders out of the track borders (i.e. $\Delta V_i = 20$ km/h), the run-off area required with $\Delta n_i = 3$ m is fully contained inside the run-off area required with $\Delta n_i = 0$ m.

Fig. 7b shows the recovery trajectories starting from the location closest to the turn apex ($s_i = 725$ m), with a negative trajectory displacement (i.e. towards the outer track border). When the speed and trajectory errors are combined, the resulting recovery trajectory results wider than the corresponding ones obtained with no lateral displacement. Nonetheless, all the recovery manoeuvres are completed within the track borders and no paved run-off area is required for this kind of driving errors.

In sum, the results suggest that the speed excess is the key parameter in estimating the required paved run-off areas, while the lateral trajectory displacements can be discarded (even when combined with a speed error).

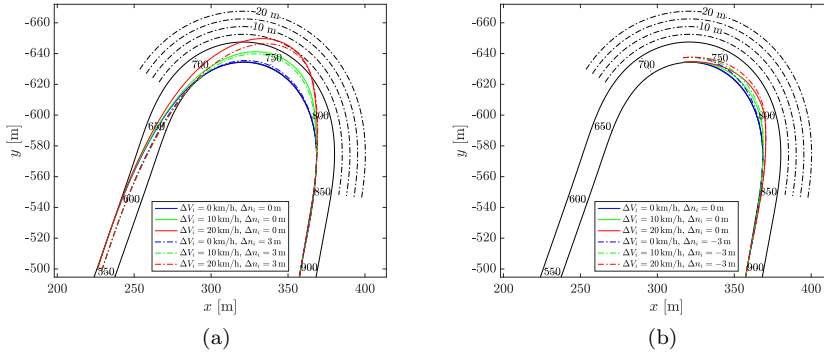


Fig. 7: Recovery trajectories from combined speed and lateral position errors on the entry of Turn 1. (a) $s_i = 550 \text{ m}$. (b) $s_i = 725 \text{ m}$.

Similar results were obtained on all the other turns of the circuit – they are not reported for conciseness of presentation.

6.4 Paved run-off areas

In this section, the results of the simulated (minimum-time) recovery manoeuvres are employed to estimate the shape of the required paved run-off areas. The idea is that the paved run-off areas should at least include the trajectory associated to the recovery manoeuvres, in order to allow the riders to recover from possible driving errors. The shape clearly depend on the track, the vehicle, and driving errors (types and magnitude).

The boundary of the run-off area is computed as the envelope of all the simulated trajectories obtained for $s_1 \leq s_i \leq s_2$, as shown in Fig. 8 for Turn 1. However, the envelope often coincides with one of the trajectories, typically the one with the rearmost starting location ($s_i = s_1$) or starting immediately after the rearmost starting location ($s_i = s_1 + 25 \div 50 \text{ m}$). As each turn is characterised by a different speed profile, and in particular a different entry speed, it is convenient to consider a relative speed excess instead of an absolute speed excess. Speed errors up to 9%, with 3% steps, are considered in this study.

Fig. 9 displays the required run-off areas for the various turns of the Mugello circuit and for the different speed errors. Only the envelopes that leave the track are shown. The run-off area corresponding to the highest speed error is also highlighted by a shaded blue area. Simulation results are overlaid on top of satellite images extracted from Google Maps, in order to compare the shape and size of the existing (at the time of satellite images) paved run-off areas and the ones obtained with the numerical simulation. It is interesting to note that the maximum widths of the existing run-off areas of the circuit analysed are

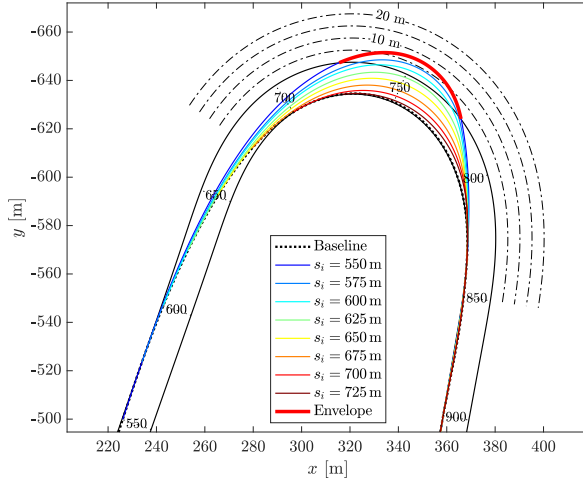


Fig. 8: Envelope of recovery trajectories from a speed error $\Delta V_i = 9\%$ on the entry of Turn 1 .

close to those computed with a 9% speed error. However, the simulations also suggest that the location of the maximum run-off area width should be shifted further from the turn entry, in order to allow the recovery with a minimum-time strategy. In most cases, a 3% speed excess can be recovered within the track borders.

The considerations related to Turn 1 hold valid for almost all of the other turns of the circuit, with few exceptions (Turns 8, 12 and 15). When allowing for the use of a paved run-off area around Turn 8, the recovery manoeuvre with a zero speed excess is faster than the baseline manoeuvre, i.e. it is always convenient to use the paved run-off area. In Turns 12 and 15 the maximum width of the paved run-off area required by the simulations for $\Delta V_i = 9\%$ is 2 to 3 times greater than the maximum width of the actual paved run-off area provided by the satellite images. Nevertheless, in these turns the retention barriers are placed quite close to the outer track border (approximately 30 m) and a wide paved area outside of the turn is probably not viable – in the event of a fall or crash there may not be enough gravel to slow down the motorcycle and the rider before they hit the barriers.

7 Conclusion

The concept of optimal recovery manoeuvre has been introduced, and associated to the manoeuvre that is necessary to perform in order to complete the lap in the minimum time, after a driving error. The latter has been defined in terms of speed excess and trajectory deviation with respect to a baseline

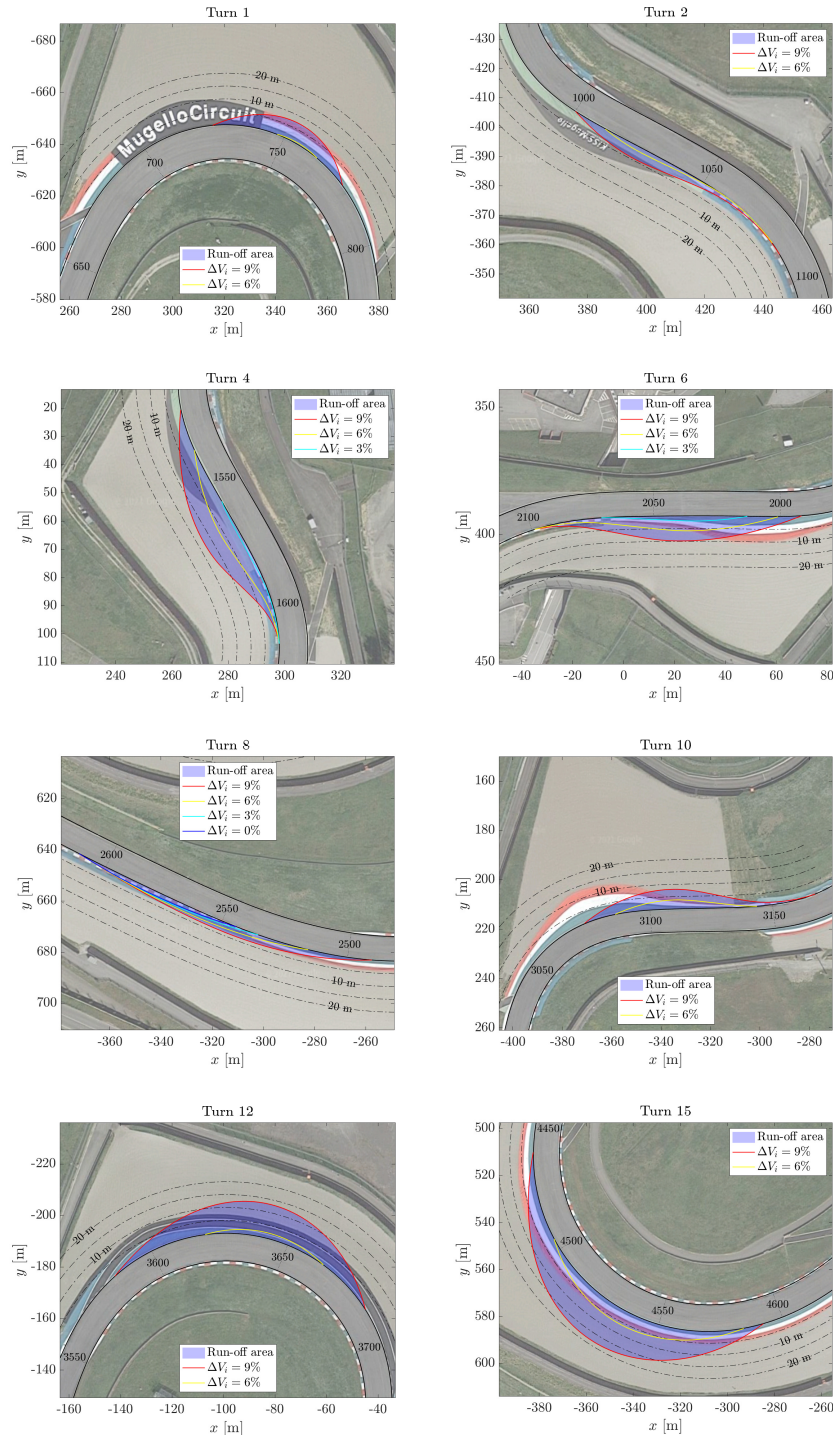


Fig. 9: Paved run-off areas required for recovery from relative speed excess.

manoeuvre, which is the minimum-lap-time manoeuvre (without driving errors). An example of application has been given for a racing motorcycle on the Mugello circuit. Speed excess proved the most relevant error when it comes to the assessment of the size and shape of the paved run-off areas. In general, the size of the run-off areas obtained as the envelope of the simulated recovery manoeuvres is comparable with that of the existing paved areas. However, the simulations also suggest a slightly different shape in order to allow the recovery with a minimum-time strategy, with the maximum run-off width shifted towards the exit of the turn. The recovery manoeuvres have been obtained within a nonlinear optimal control framework, using an indirect collocation method. The dynamic vehicle model has 20 first-order differential equations and runs on a three-dimensional track model, while the vehicle positioning is obtained through curvilinear coordinates.

8 Compliance with Ethical Standards

The authors declare that they have no conflict of interest.

References

1. Massaro M, Limebeer DJN. Minimum-lap-time optimization and simulation. *Vehicle System Dynamics*. 2021;59(7):1069–1113; Available from: <https://doi.org/10.1080/00423114.2021.1910718>.
2. Lovato S, Massaro M, Limebeer DJN. Curved-ribbon-based track modelling for minimum lap-time optimisation. *Meccanica*. 2021;56:2139–2152; Available from: <https://doi.org/10.1007/s11012-021-01387-3>.
3. Sedlacek T, Odenthal D, Wollherr D. Minimum-time optimal control for vehicles with active rear-axle steering, transfer case and variable parameters. *Vehicle System Dynamics*. 2021;59(8):1227–1255; Available from: <https://doi.org/10.1080/00423114.2020.1742925>.
4. Christ F, Wischnewski A, Heilmeier A, Lohmann B. Time-optimal trajectory planning for a race car considering variable tyre-road friction coefficients. *Vehicle System Dynamics*. 2021;59(4):588–612; Available from: <https://doi.org/10.1080/00423114.2019.1704804>.
5. Limebeer DJN, Massaro M. *Dynamics and optimal control of road vehicles*. Oxford University Press; 2018.
6. Lovato L, Massaro M. A three-dimensional free-trajectory quasi-steady-state optimal-control method for minimum-lap-time of race vehicles. *Vehicle System Dynamics*. 2021; Available from: <https://doi.org/10.1080/00423114.2021.1878242>.
7. Dal Bianco N, Biral F, Bertolazzi E, Massaro M. Comparison of Direct and Indirect Methods for Minimum Lap Time Optimal Control Problems. *Vehicle System Dynamics*. 2018;57(5):665–696; Available from: <https://doi.org/10.1080/00423114.2018.1480048>.
8. Massaro M, Marconi E. The Effect of Engine Spin Direction on the Dynamics of Powered Two Wheelers. *Vehicle System Dynamics*. 2018;56(4):604–620; Available from: <https://doi.org/10.1080/00423114.2017.1397277>.
9. Dal Bianco N, Lot R, Gadola M. Minimum time optimal control simulation of a GP2 race car. *Proceedings of the Institution of Mechanical Engineers, Part D: Journal of Automobile Engineering*. 2018;232(9):1180–1195; Available from: <https://doi.org/10.1177/0954407017728158>.
10. Limebeer DJN, Rao AV. Faster, higher, and greener: Vehicular optimal control. *IEEE Control Systems Magazine*. 2015;35(2):36–56; Available from: <https://doi.org/10.1109/MCS.2014.2384951>.

11. Limebeer DJN, Perantoni G, Rao AV. Optimal Control of Formula One Car Energy Recovery Systems. *International Journal of Control*. 2014;87(10):2065–80; Available from: <https://doi.org/10.1080/00207179.2014.900705>.
12. Tavernini D, Velenis E, Lot R, Massaro M. The Optimality of the Handbrake Cornering Technique. *Journal of Dynamic Systems, Measurement, and Control*. 2014;136(4); Available from: <https://doi.org/10.1115/1.4026836>.
13. Kelly DP, Sharp RS. Time-optimal control of the race car: a numerical method to emulate the ideal driver. *Vehicle System Dynamics*. 2010;48(12):1461–1474; Available from: <https://doi.org/10.1080/00423110903514236>.
14. Bertolazzi E, Biral F, Da Lio M. Symbolic-numeric efficient solution of optimal control problems for multibody systems. *Journal of computational and applied mathematics*. 2006;185(2):404–421; Available from: <https://doi.org/10.1016/j.cam.2005.03.019>.
15. Casanova D, Sharp RS, Symonds P. Sensitivity to mass variations of the fastest possible lap of a formula one car. *Vehicle system dynamics*. 2001;35(2):119–134.
16. Metz D, Williams D. Near Time-Optimal Control of Racing Vehicles. *Automatica*. 1989; 25(6):841–57; Available from: [https://doi.org/10.1016/0005-1098\(89\)90052-6](https://doi.org/10.1016/0005-1098(89)90052-6).
17. Hendrikx JPM, Meijlink TJJ, Kriens RFC. Application of Optimal Control Theory to Inverse Simulation of Car Handling. *Vehicle System Dynamics*. 1996;26(6):449–61; Available from: <https://doi.org/10.1080/00423119608969319>.
18. Scherenberg H. Mercedes-Benz Racing Design and Cars Experience. *SAE Transactions*. 1958;(580042):414–20; Available from: <https://doi.org/10.4271/580042>.
19. Pacejka HB. *Tire and vehicle dynamics*. 3rd ed. Oxford: Butterworth Heinemann; 2012.
20. Cossalter V. *Motorcycle dynamics*. Lulu; 2006.
21. Leonelli L, Limebeer DJN. Optimal control of a road racing motorcycle on a three-dimensional closed track. *Vehicle System Dynamics*. 2020;58(8):1285–1309; Available from: <https://doi.org/10.1080/00423114.2019.1617886>.
22. Marconi E, Massaro M. The effect of suspensions and racetrack three-dimensionality on the minimum lap time of motorcycles. *Lecture Notes in Mechanical Engineering*. 2020; :1368–1377.
23. Nozad A, Lidberg M, Gordon T, Klomp M. Optimal path recovery from terminal understeer. In: *IAVSD Symposium*, Manchester, UK; 2011.
24. Gordon TJ, Klomp M, Lidberg M. Strategies for minimizing maximum off-tracking resulting from over-speed in curves. In: *Proceedings of 11th International Symposium on Advanced Vehicle Control (AVEC)*, Seoul Korea; 2012.
25. Klomp M, Lidberg M, Gordon TJ. On optimal recovery from terminal understeer. *Proceedings of the Institution of Mechanical Engineers, Part D: Journal of Automobile Engineering*. 2014;228(4):412–425; Available from: <https://doi.org/10.1177/0954407013511796>.
26. Gao Y, Gordon T. Optimal control of vehicle dynamics for the prevention of road departure on curved roads. *IEEE Transactions on Vehicular Technology*. 2019;68(10):9370–9384; Available from: <https://doi.org/10.1109/TVT.2019.2927333>.
27. Cossalter V, Lot R, Massaro M. An Advanced Multibody Code for Handling and Stability Analysis of Motorcycles. *Meccanica*. 2011;46:943–58; Available from: <https://doi.org/10.1007/s11012-010-9351-7>.
28. Massaro M, Lot R, Cossalter V. On Engine-to-Slip Modelling for Motorcycle Traction Control Design. *Proceedings of the Institution of Mechanical Engineers, Part D: Journal of Automobile Engineering*. 2011;225(1):15–27; Available from: <https://doi.org/10.1243/09544070JAUTO1575>.
29. Lot R. A motorcycle tire model for dynamic simulations: Theoretical and experimental aspects. *Meccanica*. 2004;39(3):207–220; Available from: <https://doi.org/10.1023/B:MECC.0000022842.12077.5c>.

Appendix

The following Tab. 1 reports the dataset employed for the simulations of Sec. 4 and Sec. 6.

Table 1: Vehicle dataset.

Whole vehicle geometry and inertia	
Vehicle mass	250 kg
Height of centre of mass	0.69 m
Longitudinal distance of centre of mass from rear axle	0.73 m
Wheelbase	1.5 m
Normal trail	0.1 m
Caster angle	0.45 rad
Moment of inertia about the x -axis	18 kg m ²
Moment of inertia about the y -axis	50 kg m ²
Moment of inertia about the z -axis	40 kg m ²
Product of inertia ($I_{xz} = \int xzdm$)	-2 kg m ²
Front frame inertia	
Front frame mass	30 kg
Height of centre of mass	0.55 m
Longitudinal distance of mass centre from rear axle	1.36 m
Moment of inertia about the z -axis (steer)	0.48 kg m ²
Rear wheel and tyre	
Unsprung mass	25 kg
Spin inertia	0.67 kg m ²
Tyre radius	0.33 m
Tyre crown section radius	0.095 m
Tyre normal stiffness	154 kN/m
Tyre radial stiffness	154 kN/m
Tyre lateral stiffness	100 kN/m
Sideslip stiffness per unit load	15 rad ⁻¹
Roll stiffness per unit load	0.8 rad ⁻¹
Relaxation length	0.15 m
Longitudinal friction coefficient	1.3
Lateral friction coefficient	1.4
Front wheel and tyre	
Unsprung mass	11 kg
Spin inertia	0.41 kg m ²
Tyre radius	0.30 m
Tyre crown section radius	0.06 m
Tyre normal stiffness	157 kN/m
Tyre radial stiffness	157 kN/m
Tyre lateral stiffness	108 kN/m
Sideslip stiffness per unit load	13 rad ⁻¹
Roll stiffness per unit load	0.9 rad ⁻¹

Continued on next page

Table 1 – *Continued from previous page*

Relaxation length	0.12 m
Longitudinal friction coefficient	1.35
Lateral friction coefficient	1.4
Aerodynamics	
Drag area coefficient (acceleration)	0.2 m^2
Drag area coefficient (deceleration)	0.5 m^2
Lift area coefficient	0.05 m^2
Height of centre of pressure	0.51 m
Longitudinal distance of centre of press. from rear axle	0.74 m
Suspensions	
Rear vertical stiffness	30 kN/m
Rear vertical damping	3.5 kNs/m
Front stiffness	30 kN/m
Front damping	3.5 kNs/m
Constraints	
Engine maximum power	160 kW
Maximum steering angle	0.2 rad
Maximum handlebar torque	200 Nm